LANGMUIR

Article

pubs.acs.org/Langmuir

Binary Colloidal Crystal Films Grown by Vertical Evaporation of Silica Nanoparticle Suspensions

Jennifer L. Russell, Grace H. Noel, Joseph M. Warren, Ngoc-Lan L. Tran, and Thomas E. Mallouk*

Departments of Chemistry, Biochemistry and Molecular Biology, and Physics, The Pennsylvania State University, University Park, Pennsylvania 16802, United States

Supporting Information

ABSTRACT: Despite intensive research efforts in the synthesis of binary colloidal crystals, the production of well ordered binary colloidal crystal films over large areas continues to be synthetically challenging. In this paper, we investigate the phase behavior of binary mixtures of L-arginine-stabilized 36 and 22 nm silica nanoparticles deposited as centimeter-scale thin films onto a vertical substrate via evaporative assembly. By adjusting the temperature and relative colloid composition under high humidity conditions, we controlled the order of the resultant colloidal crystal films. The domain size of the AB_2 binary crystalline phase increased with an excess of small (B) particles and a very slow evaporation rate below 45 °C, with the best results obtained at 30° and 35 °C.

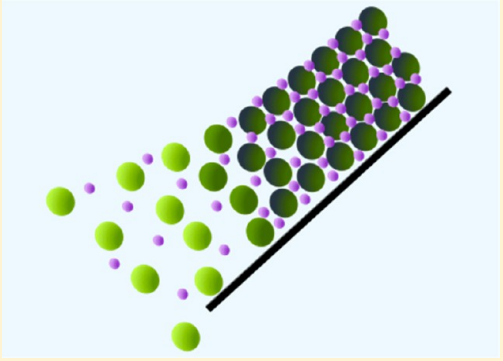

INTRODUCTION

First noted in natural Brazilian opals by Sanders in 1980, binary colloidal crystals are ordered structures derived from the coassembly of two different particles that differ by either size, charge, and/or composition.[1,2] In the pursuit of shrinking periodic dimensions, there is an ongoing interest in binary colloidal crystals made from nanoparticles, the structural diversity of which enables several applications.[3,4] For instance, in the race to produce complete photonic bandgap materials, binary colloidal crystals were found to have potentially wider bandgaps than single-size colloid crystals.[5] Binary colloidal crystals are also a platform for sensing applications, templates for novel inverse structures, superhydrophobic surfaces, exotic crystal growth (quasicrystals, rare superstructures), and surface plasmon-enhanced properties.[5−14]

Multiple successful approaches have been reported for assembling colloidal crystals, such as horizontal evaporation,[15,16] electric field,[17,18] layer-by-layer assembly,[19] vertical evaporative deposition (with and without substrate withdrawal),[11,20,21] spin-coating,[22] floating monolayers,[23] and template/pattern assistance.[24−27] Vertical evaporation is the slowest method, but it is simple, is scalable, and produces high quality colloidal crystals when the evaporation rate is slow relative to the crystal nucleation rate. In vertical evaporative assembly, colloids flow to the air/solvent interface via the evaporative flux. Capillary forces pull the nanoparticles together in the forming interfacial layer, followed by transfer to substrate as evaporation progresses in the final drying step.[28,29]

Optimal unary and binary colloidal deposition conditions vary necessarily according to solvent and colloid size/ratio composition.[30−35] A systematic study of conditions for each system is necessary for reproducibility and for a better understanding of binary colloidal assembly. Intensive efforts have gone into binary crystal phase modeling, microparticle assembly, and bulk growth,[36−44] but the field of binary nanoparticle film deposition is still in the early stages of development. Colloidal crystal film growth, in contrast to bulk growth, yields a supported material for device applications or physical property measurements that utilize the support. Crystal growth deposition as a thin film can also provide epitaxial control over growth through templating or layer-by-layer assembly.[19] Large-scale depositions of crystalline films from 10s of nanometer size particles present additional challenges relative to the heavily studied assembly of micron-sized spheres due to synthetic limitations, higher polydispersity, and shape anisotropy. Therefore, there is an ongoing need to better understand binary nanocrystal deposition in order to bridge the material size gap between atomic and microscale periodicity.

In this work, we performed vertical evaporative deposition of centimeter-scale binary silica nanoparticle films onto stationary silicon wafers. Using a high humidity chamber (customized vacuum oven in Figure 1), films of varying number ratios of 35.7 ± 2.0 nm and 22.4 ± 1.7 nm diameter silica spheres were deposited in the temperature range 30−55 °C to determine the optimal conditions for growing the largest binary crystalline domains across a sample. At this size ratio (small/large) of 0.627 ± 0.059, the most stable binary crystalline phases, according to previous hard sphere packing calculations, are AB_2 (most thermodynamically favorable) and AB_{13}.[34] We used

Received: July 21, 2017
Revised: September 5, 2017
Published: September 6, 2017

DOI: 10.1021/acs.langmuir.7b02553
Langmuir 2017, 33, 10366−10373

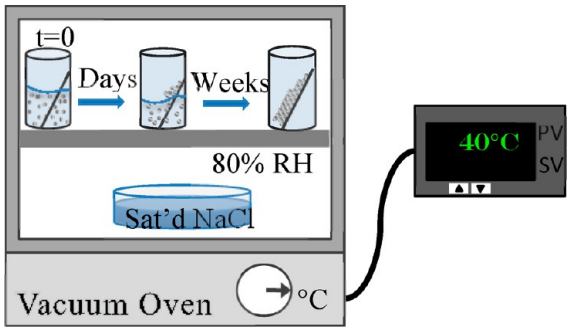

Figure 1. Vertical evaporative assembly experimental setup.

amino acid-stabilized silica nanoparticles in the 10s of nanometer size regime. Amino acid-catalyzed silica synthesis, as initially described by Yokoi and Davis,[45,46] yields spherical, monodisperse silica nanoparticles that readily crystallize upon evaporation.[47]

EXPERIMENTAL SECTION

Silica colloid synthesis. Silica nanoparticles of 31−36 nm and 20−22 nm diameters were prepared by following the Hartlen method.[48] In brief, 22.4 ± 1.7 nm diameter particles were prepared by gently stirring a mixture of 0.52 mmol L-arginine (Sigma-Aldrich, ≥ 98%) and 3.8 mol nanopure water below a floating layer of 0.042 mol cyclohexane (anhydrous, 99.5%) and 0.025 mol tetraethyl orthosilicate (Sigma-Aldrich, 98%). This biphasic mixture was reacted for 20 h at 60 °C. The reaction yielded the 22 nm seed silica particles, which had formed and remained suspended in the higher density aqueous-arginine phase. The reaction flask was cooled to room temperature and then the aqueous seed phase was collected by pipet, separating it from the immiscible floating cyclohexane-unreacted TEOS phase. 35.7 ± 2.0 nm nanoparticles were prepared by mixing 20 mL of the freshly prepared seed-arginine solution with 4.0 mol nanopure water and with a floating layer of 0.031 mol tetraethyl orthosilicate and 0.093 mol cyclohexane. This was further reacted for 30 h at 60 °C. Adjustments in reaction time by 3−4 h less yielded the slightly smaller 20 and 31 nm colloids.

Preparation of colloidal suspensions. All colloidal suspensions were used without further purification and diluted with nanopure water (Barnstead, 18.2 MΩ cm) prior to film deposition. For binary colloids, each size colloidal suspension was diluted 7.5 times with water prior to mixing. This gave a volume fraction of 5.3×10^{-4} for 35.7 ± 2.0 nm and 7.2×10^{-4} for 22.4 ± 1.7 nm silica spheres at this dilution prior to mixing. A density of 2.04 g/cm^3 was used for silica number density calculations.[52] At this dilution, the 22 nm colloidal solution had a pH of 9.39 ± 0.01 and the 36 nm solution had a pH of 8.39 ± 0.02. Binary colloidal suspensions were prepared by thoroughly mixing smaller and larger silica nanoparticles by volume to achieve the desired number ratios. Number densities of each particle size were determined by measuring the dry mass from a known volume of colloidal suspension. Number densities are slightly underestimated due to the L-arginine content of the colloids.

The dilution factor is important to film quality, and the optimum value was determined through trial and error under laboratory conditions. Vertical deposition naturally sets up a concentration gradient as evaporation progresses and colloidal particles are driven to the solid−liquid meniscus. A higher colloid concentration results in thicker films early on that crack and delaminate once the film reaches a critical thickness of about 1.5 μm. More dilute suspensions result in incomplete coverage and extended sub- and monolayer regions at the leading edge of the film. At the optimized concentration, the useful film area was 1.0 cm × 1.0−1.5 cm long before the film became too thick and delaminated at the end.

Film deposition. Colloidal crystal films were assembled using static vertical evaporation. Dry silicon substrates were slanted approximately 30° from the vertical direction in open plastic cylindrical vials. Each vial was filled with a colloidal suspension and then placed in a humidity- and temperature-controlled vacuum oven chamber (Figure 1). The temperature was controlled and calibrated with an Athena PID temperature process controller and a thermocouple affixed inside the oven. In-oven temperature and humidity were monitored with a Lascar USB temperature and humidity data logger. Based on literature and preliminary experiments, we found that the best colloidal crystal films were deposited in high (≥75%) humidity.[49,50] Low humidity depositions resulted in thick, cracked, and delaminated films. High humidity produced smooth, large area films (Figure 2). We controlled humidity to within 80−85% by

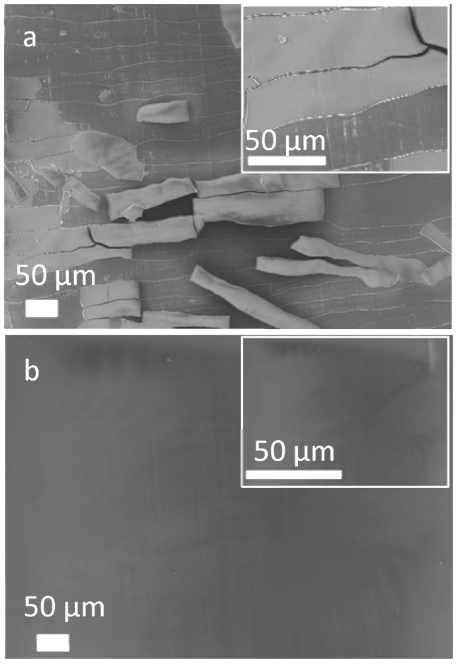

Figure 2. (a) Scanning electron microscopy (SEM) image of a 30 nm colloidal crystal deposited in low (5%) humidity at 40 °C. (b) Same colloid deposited in high 80% humidity at 40 °C.

placing a crystallizing dish filled with saturated aqueous NaCl in the deposition chamber.[51] The evaporation rate varied from 5.9 ± 0.5 × 10^{-6} mm/s at 30 °C to 2.6 ± 0.3 × 10^{-5} mm/s at 55 °C. Temperature was controlled within 0.5 °C.

Colloidal suspensions were then allowed to evaporate undisturbed for 1−6 weeks, depending on the evaporation temperature/rate. Disturbing the deposition chamber, for example opening the oven door briefly to check the progress of film deposition, caused an immediate drop in humidity and disruption of crystal growth that was visible to the naked eye as a change in the film interference color (Figure 3).

Substrate preparation. P-type ⟨100⟩ silicon wafers (1−10 Ω-cm with native oxide layer present, obtained from University Wafer) were cleaved into approximately 2.5 cm × 1.0 cm rectangular size. The wafers were immersed in freshly prepared piranha solution (3:1 concentrated sulfuric acid and 30% v/v hydrogen peroxide) for 30 min to clean the surface and to render the wafers sufficiently hydrophilic. [**Caution**: piranha solution is dangerous and reacts violently with organic substances!] The cleaned wafers were rinsed copiously with nanopure water and stored in nanopure water until immediately before use.

Characterization. Colloidal particles were sized and films imaged by scanning electron microscopy using a Zeiss SIGMA VP-FESEM. At least 100 particle diameters were measured for each particle size distribution. We imaged all films without using metal coatings.

DOI: 10.1021/acs.langmuir.7b02553
Langmuir 2017, 33, 10366−10373

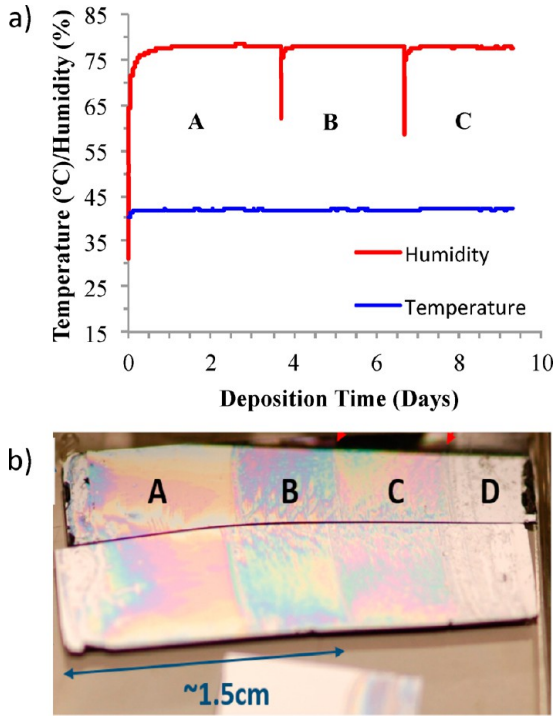

Figure 3. (a) Humidity and temperature reading for the first 9.5 days of film deposition. Spikes in humidity were due to briefly opening the deposition chamber. (b) Photograph of the resulting film showing the visible disruptions in growth at intervals corresponding to humidity drops. Part D is the thick, delaminating bottom portion of the film.

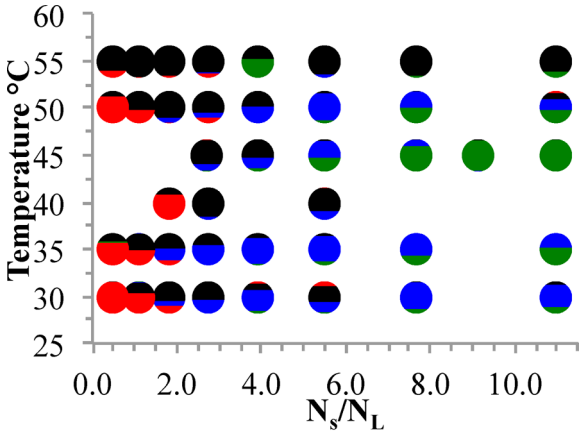

Color	Phase
Black	Disordered
Red	FCC 36 nm
Green	FCC 22 nm
Blue	AB_2

Figure 5. Phase mapping for AB_2 binary mixtures of 36 nm (A) and 22 nm (B) silica nanoparticles; N_s/N_L = particle number density ratio of small-sized particles to larger-sized particles. Colors in circles reflect the relative populations of the corresponding phases.

RESULTS AND DISCUSSION

Binary colloidal crystal phase map. Figures 4 and 5 summarize the colloidal crystal film phases observed under the conditions tested. A table and additional phase plots summarizing the results are in the Supporting Information (Table S1 and Figure S1). The diagram in Figure 5 is color-coded according to the phases observed; the relative amounts of each phase are reflected in the proportion of colors in each circle. Some phases were present in amounts too small to be represented this way; therefore we refer to Table S1 of the Supporting Information for more detail. Phases in the map were determined from an average of 30 or more 5 μm^2 areas sampled via SEM observations in the leading ~1.5 cm of the film since the film thickens to the point of cracking/delaminating beyond this point. The relative amounts of phases were reported based on the area occupied by each phase in the sampled 5 μm^2 areas. Areas were sampled by rastering horizontally across the film and imaging 3−5 regions, followed

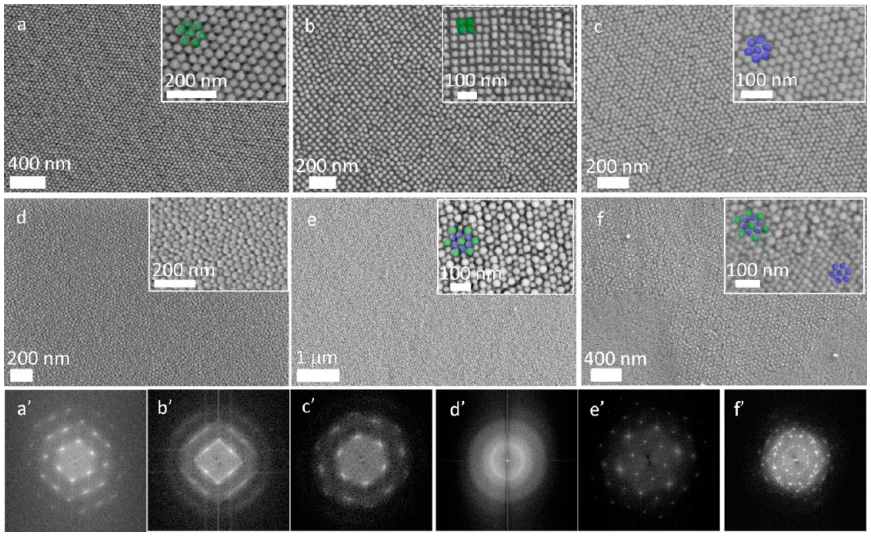

Figure 4. (a) fcc (111) exposed face of 36 nm phase at 50 °C and N_s/N_L = 0.5, (b) fcc 36 nm phase with exposed (100) face at 30 °C and N_s/N_L = 0.5, (c) fcc 22 nm phase (with (111) exposed plane top surface) at 30 °C and N_s/N_L = 3.9, (d) disordered packing of A and B at 35 °C and N_s/N_L = 1.1, (e) large AB_2 domain (>16 μm^2) from 30 °C and N_s/N_L = 11.0, (f) small AB_2 domains surrounded by the fcc 22 nm phase from 45 °C and N_s/N_L = 7.7. Note: light surface cracking in images is due to the electron beam during imaging. Bottom row images a′ through f′ are FFT patterns of images a though f, respectively.

DOI: 10.1021/acs.langmuir.7b02553
Langmuir 2017, 33, 10366−10373

by shifting down the sample incrementally and repeating. The concentration gradient that evolves during deposition has a small effect on the phases observed. Crystalline domains tend to extend to larger regions after the film begins to deposit along the growth direction. Phase behavior along the growth direction depends on the relative amounts of each phase and the domain sizes. Coexisting phases tend to be present throughout the films in either alternating banded regions along the length of the sample, or they may mix in a patchwork fashion (especially common with smaller domain sizes). Phases existing in small patches or in rare isolated regions appear as very low (<5%) percentages in Table S1.

Additionally, samples were dissected and imaged via cross-sectional SEM to verify that the same phases were present throughout the film. Most often, the phases seen at the surface persisted through the cross-section down to the substrate. Occasionally, the phases observed on the surface alternated in layers in the interior of the film. Additional images of cross sections are provided in the Supporting Information (See Figure S3). Fast Fourier transform (FFT) images were provided for all images in Figure 4 to demonstrate presence of long-range order or disorder. Additional comparison between the FFT of a drawn AB_2 diagram and experiment are compared in Figure S3 of the Supporting Information.

At the left edge of the diagram in Figure 5, at N_s/N_L = 0.5 and 1.1, the fcc 36 nm phase dominated with variable amounts of disordered binary regions (Figure 4a). For N_s/N_L = 0.5 at 30 and 35 °C, a significant portion of the fcc 36 nm phase preferentially oriented with the (100) plane on the top surface (Figure 4b). Larger Ns/N_L ratios starting at 5.5 and above (Figure 4c) yield larger amounts of the 22 nm close packed phase because this size is increasingly in excess. Unary films typically orient with the low energy hexagonal (111) face exposed. In films with majority unary phases, the minority particle population of the other size is usually present as dispersed point defects; but they can also segregate into isolated unary phase islands or line the grain boundary perimeters of the majority particle phase.

Deposition at 55 °C resulted in mostly disordered binary mixtures (Figure 4d) between N_s/N_L = 2.3 and 11.0, which is likely due to faster evaporation relative to crystal growth at this higher temperature. At 55 °C, disordered packings were also common at lower N_s/N_L where there was a higher concentration of 36 nm particles but still enough 22 nm particles to compete with fcc 36 nm crystallization. Regions of AB_2 packing were found in most films between N_s/N_L = 1.8 and 11.0 at growth temperatures below 55 °C. AB_2 regions ranged from large domains spanning 10s of microns (Figure 4e) to much smaller island type domains surrounded by a perimeter of unary phase or disordered mixture (Figure 4f).

We expected to find the AB_2 phase predominantly near a stoichiometric 2:1 ratio of particles in the deposition mixture, i.e., near N_s/N_L = 2.0; however, films enriched in the largest domains/coverage of AB_2 occurred at N_s/N_L = 3.9 and 5.9 for growth temperatures between 30 and 50 °C. Deposition at 30 °C produced the largest domains (>15 μm^2) and significant AB_2 coverage at N_s/N_L = 7.7 and 11.0 (Figure 6).

At higher temperatures in the higher N_s/N_L region of Figure 5, the 22 nm fcc phase increases in coverage in the films prior to widespread disordering at the highest temperatures. This shift from larger AB_2 domains to fcc 22 nm at higher temperature suggests faster growth of the fcc phase relative to the AB_2 phase. The observation of larger crystalline domains at

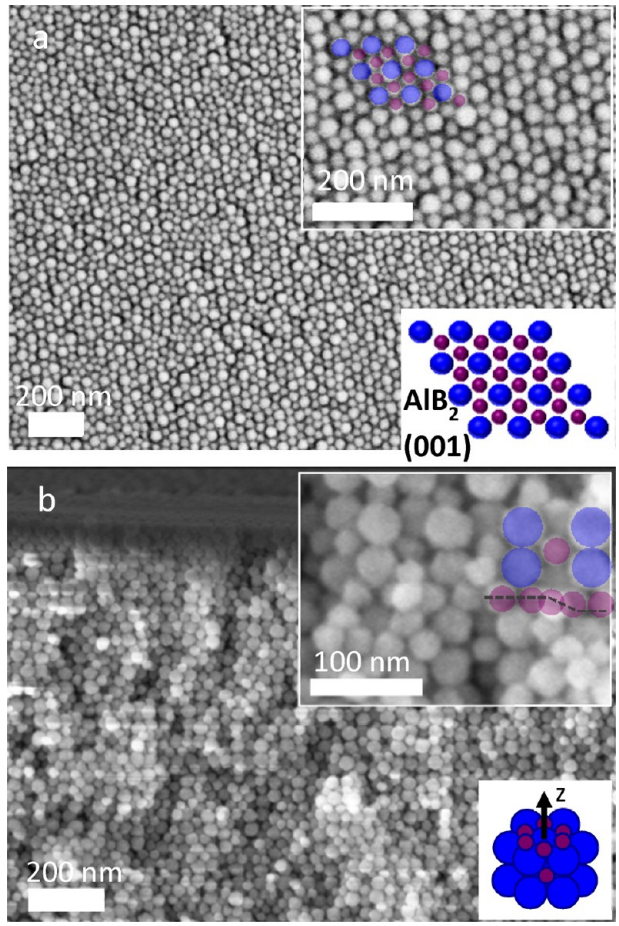

Figure 6. (a) Top view SEM of AB_2 lattice and (b) cross section. 30 °C N_s/N_L = 11.0; inset shows repeat pattern which zig-zags in and out of plane. This appears to face the (111) plane at an angle, but the material fractures in such a way that multiple layers are exposed. Microcracks on the top surface in part a reflect damage that occurs under the electron beam.

lower deposition temperature aligns with expectations that the complicated binary lattice grows under conditions of low supersaturation, i.e., when nucleation of new crystal grains is slow. Higher temperature depositions yielded smaller, polycrystalline domains more often until binary order was no longer observed at 55 °C by SEM.

The particle size ratio of 0.627 is at the edge of stability for two binary phases, AB_{13} and AB_2. Based on packing considerations alone, AB_2 should be the more thermodynamically favorable structure, as it is the closest packed binary phase, followed closely by AB_{13}.[34,52,53] Despite their closeness in energy, AB_2 was the only binary crystalline phase observed in these two sphere sizes. The stability of AB_{13} and AB_2 lattices in the ~0.6 size ratio regime has been intensively studied because the most thermodynamically favorable binary structure has not always been the experimentally observed product, even under near-equilibrium growth conditions. In some cases AB_{13} has been observed instead of AB_2, or a fluid type phase predominated. It has been postulated that crystallization kinetics play a significant role in phase selection.[52−56] At the nearby size ratios of 0.61 and 0.625 (within our size ratio error) under constant volume conditions, Bartlett and Eldridge experimentally and by simulation observed a suppression of the AB_2 phase, which appeared to grow more slowly than AB_{13}.

DOI: 10.1021/acs.langmuir.7b02553
Langmuir 2017, 33, 10366−10373

At size ratio of 0.625, equilibrium phase diagrams predicted only AB_{13} as the crystalline binary phase.[53,56] However, our slow vertical evaporation conditions allowed AB_2 to crystallize readily over a range of particle number fractions. It is possible that AB_{13} might occur with an even greater excess of 22 nm silica spheres since our experiments were carried out below the 13:1 stoichiometry; but at values of N_s/N_L above 4.0 we observe increasing amounts of the fcc 22 nm phase.

Size ratio and particle volume fractions determine the thermodynamically stable phases for a colloidal mixture, but the method of colloidal crystallization can have a striking effect on the experimental results. Vertical evaporation, unlike constant volume crystallization, involves the flux of particles from a dilute suspension to an interface where they condense and rearrange before depositing as a solid onto the substrate. Capillary forces and electrokinetic effects may alter the ratio of sphere sizes in the meniscus, where the particle concentration becomes high enough for crystal nucleation and growth. Some additional chemical effects may contribute to nucleation of a particular crystal phase. We have found (details will be reported elsewhere) that arginine-capped silica particles do not pack as hard spheres but can actually change their shape somewhat in colloidal crystals in order to maximize crystal density. Silica spheres can also form bridges between neighboring surfaces upon dehydration (see Figure S4 in the Supporting Information), which may promote the nucleation of certain crystal phases. Adjusting the ionic strength by additions of sodium chloride to the depositing solution had small to severe effects on long-range ordering (see Figure S5 in the Supporting Information) but did not lead to the crystallization of binary phases other than AB_2.

Deposition of single-size colloid films. In order to better understand the colloid depletion effects that accompany evaporation/deposition on the phase behavior in binary mixtures, we systematically studied the deposition of two different sized silica particles (30.8 ± 2.3 nm and 20.3 ± 1.6 nm) into their respective unary films. We looked at the two sizes separately in order to deconvolute the size-dependent deposition rates from the complicated behavior of the binary mixture. Data points were obtained at the same volume concentration of each size, meaning that the solution number density was always higher by a factor of $(30.8/20.3)^3 = 3.49$ for the smaller particles. Film thickness measurements were obtained by cross-sectional SEM at the center of the film and 5.0 mm from the leading edge. Samples were cross-sectioned twice 90° apart in order to account for local thickness variations in the x and y directions about the points of interest. Since the meniscus shape is affected by the deposition angle and the film thickness increases as growth proceeds, all solutions were deposited on the same size/angled (approximately 30 degrees from the normal) substrate with the same starting solution height.

Figure 7 plots film thickness as a function of colloid concentration at 45 °C, and Table 1 compares the number ratio in the solution with the layer number ratio of small vs large particles deposited in the films. The layer number ratio was determined from the measured film thicknesses and known particle diameters. As anticipated from ref 20, the film thickness increases with initial bulk particle concentration in a linear fashion. The lines in Figure 7 extrapolate to within ~1−1.5 particle diameters of the origin. The deviations from the origin likely come from errors accrued in the thickness measurement and local film thickness variations. The 20 nm films were

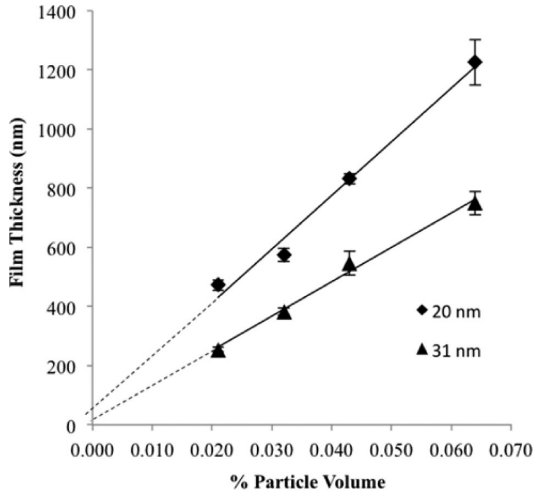

Figure 7. Film thickness vs %particle volume in solution for unary films derived from 20.3 and 30.8 nm diameter silica particles.

Table 1. Solution/Film Number Density Comparison from Film Thickness Measurements 5 mm from the Leading Edge

Particle volume %	N_{small}/N_{large} in solution	N_{small}/N_{large} in film	$(N_{S,film}/N_{L,film})/(N_{S,soln}/N_{L,soln})$
0.021	3.49	2.81	0.81
0.032	3.49	2.27	0.65
0.043	3.49	2.30	0.66
0.064	3.49	2.48	0.71

thicker than those grown from 31 nm particles because their solutions have a higher number density by a consistent factor of 3.49. The slopes of the lines indicate that over the range of particle concentrations studied, the number ratio of small to large particles (N_s/N_L) was lower in the deposited unary films than in the bulk solution. This is consistent with the observation that solution N_s/N_L ratios are higher than those in the binary colloidal crystal films that are grown from them. This trend is shown in Figure 5, where the optimum N_S/N_L ratio for obtaining the AB_2 phase is significantly higher than 2.0.

Size segregation in binary colloid films. The vertically evaporated films showed weak size segregation at the leading edge. Growth of the bulk film is preceded by a submonolayer "island" region, which is formed in the meniscus that rises up the hydrophilic substrate. These islands are large isolated collections of particles in round or band shapes surrounded by bare substrate, which always consist of an ordered band of small nanoparticles surrounding a region rich in larger nanoparticles (Figure 8a). The monolayer of small particles rapidly progresses to a multilayer containing both large and small particles (Figure 8b). The initial film always leads with a band of small particles pressing on a band rich in larger particles. These bands may alternate a few times; but consistently with the small size phase pressing on the larger sizes.

Yamaki et al. and Fortini et al. modeled and experimentally studied the size segregation phenomenon of drying binary colloidal suspensions on horizontal substrates. They explained their observations in terms of convection/capillary forces and the osmotic pressure gradient. They found that size segregation occurred most readily in lower concentration dispersions, with slow evaporation, and with larger size differences between particles. In all cases, the smaller particles press upon a phase enriched in larger particles.[57,58] This was most apparent in our

DOI: 10.1021/acs.langmuir.7b02553
Langmuir 2017, 33, 10366−10373

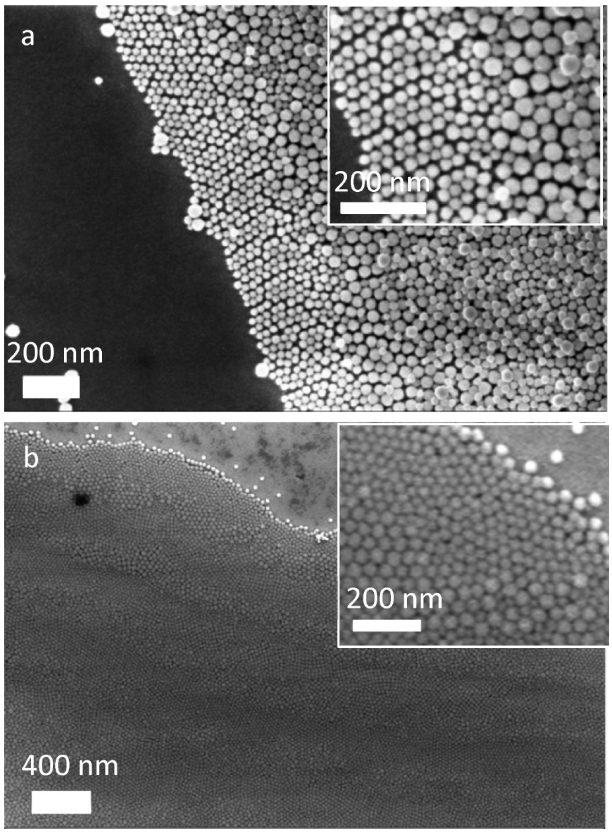

Figure 8. (a) Start of a film front leading with small particles and (b) an "island" perimeter. The drying front moves toward the bottom in both images. 36 and 22 nm particles, ratio N_s/N_L = 11.0.

system around the perimeters and submonolayer islands in the "pre-film" phase. The smaller difference between the particle sizes in our films makes stratification less effective, but it still occurs. This phenomenon demonstrates yet another complicating factor that could alter the ratio of large and small particles in binary crystal films grown by evaporative assembly.

Application to other binary films. Binary films with different size ratios can also be grown from L-arginine capped silica nanoparticles. It is relevant to note that in these other cases, the realm of stability for binary phases has expanded or shifted just beyond that reported in the literature under different deposition conditions. At size ratio 0.469, AB_{13} should not be thermodynamically stable.[34,53] However, using vertical evaporation, AB_{13} coexists with fcc regions of the smaller (B) particles (Figure 9). The reason for the deviation from hard sphere packing model predictions is not clear, but it could be due to factors noted above such as interparticle bridging and localized particle deformations in tightly packed arrangements. At larger size differences with N_s/N_L = 0.319, we encountered conditions under which several phases were formed (Figure 10), including unidentified superlattices as well as AB-, AB_2-, and AB_6-types. Figure 10b shows a pervasive, unidentified superlattice consisting of pentagonal arrangements of small spheres, but it lacks the icosahedral large-sphere ordering characteristic of the cubic AB_{13} phase.

CONCLUSIONS

Binary silica colloidal crystals with a size ratio of 0.627 were assembled over a range of temperatures and number fractions in order to optimize AB_2 crystal film growth over a centimeter-scale substrate. The best deposition conditions were found to be at 30 and 35 °C and at small/large sphere number ratios in excess of 3.0. The formation of the AB_2 phase under these conditions is consistent with the different growth rates of pure A and B films, which showed faster deposition of larger spheres. The crystal phases obtained were different from those previously reported from constant volume growth experiments and from closest packing theoretical considerations. The concentrating effect of evaporation-induced assembly, as well as kinetic effects from capillary forces, osmotic, and electrokinetic forces, and nanoparticle surface chemistry may contribute to the observed phase behavior. In crystallization via slow vertical evaporation, L-arginine capped silica colloids formed primarily phase-separated fcc and AB_2 phases at size ratios where AB_{13} should also be energetically favorable based on packing considerations alone. Additionally, vertical evaporation has the potential to draw out some exotic (and probably metastable) phases that to the best of our knowledge are so far unknown.

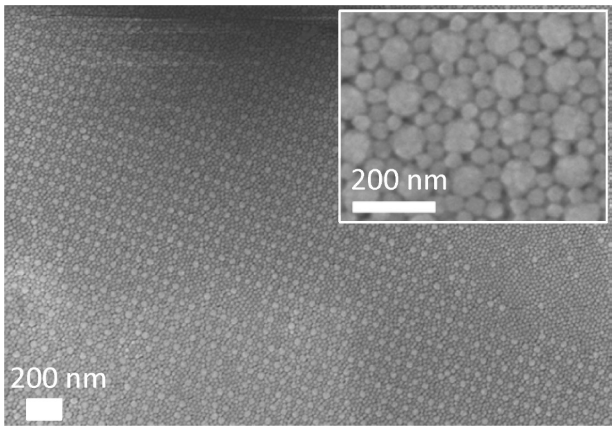

Figure 9. AB_{13} lattice grown from 41.6 ± 2.8 and 19.5 ± 1.6 nm L-arginine capped silica spheres.

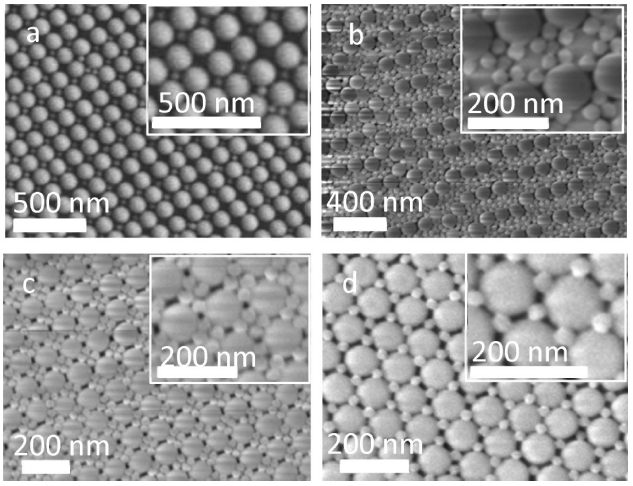

Figure 10. Ratio 0.319, 122.1 ± 3.0 nm, and 38.9 ± 2.5 nm: (a) AB-type; (b) Unknown; (c) AB_6-type; (d) AB_2.

ASSOCIATED CONTENT

Supporting Information

The Supporting Information is available free of charge on the ACS Publications website at DOI: 10.1021/acs.langmuir.7b02553.

DOI: 10.1021/acs.langmuir.7b02553
Langmuir 2017, 33, 10366−10373

Additional figures and tables detailing film growth results, and results of crystallization experiments with added salt (PDF)

AUTHOR INFORMATION

Corresponding Author

*E-mail: tem5@psu.edu.

ORCID

Thomas E. Mallouk: 0000-0003-4599-4208

Notes

The authors declare no competing financial interest.

ACKNOWLEDGMENTS

This work was supported by the National Science Foundation under MRSEC grant number DMR-1420620. We thank Darrell Velegol and Rajarshi Guha (Pennsylvania State University), Christopher Murray (University of Pennsylvania), and Michael Howard and Athanassios Panagiotopoulos (Princeton University) for valuable discussions. We also acknowledge Hiu Yan Cheng (Pennsylvania State University) for assistance with preparation of Figure 3.

ABBREVIATIONS USED

fcc, face-centered cubic; N_s, number density of small particles; N_L, number density of large particles; SEM, scanning electron microscopy

REFERENCES

(1) Sanders, J. V. Close-packed structures of spheres of two different sizes I. Observations on natural opal. *Philos. Mag. A* **1980**, *42*, 705–720.

(2) Bartlett, P.; Campbell, A. I. Three-dimensional binary superlattices of oppositely charged colloids. *Phys. Rev. Lett.* **2005**, *95*, 128302–4.

(3) Shevchenko, E. V.; Talapin, D. V.; Kotov, N. A.; O'Brien, S.; Murray, C. B. Structural diversity in binary nanoparticle superlattices. *Nature* **2006**, *439*, 55–59.

(4) Claridge, S. A.; Castleman, A. W., Jr; Khanna, S. N.; Murray, C. B.; Sen, A.; Weiss, P. S. Cluster-assembled materials. *ACS Nano* **2009**, *3*, 244–255.

(5) Wan, Y.; Cai, Z.; Xia, L.; Wang, L.; Li, Y.; Li, Q.; Zhao, X. S. Simulation and fabrication of binary colloidal photonic crystals and their inverse structures. *Mater. Lett.* **2009**, *63*, 2078–2081.

(6) Burkert, K.; Neumann, T.; Wang, J.; Jonas, U.; Knoll, W.; Ottleben, H. Automated preparation method for colloidal crystal arrays of monodisperse and binary colloid mixtures by contact printing with a pintool plotter. *Langmuir* **2007**, *23*, 3478–3484.

(7) Malekpourkoupaei, A.; Kostiuk, L. W.; Harrison, D. J. Fabrication of binary opal lattices in microfluidic devices. *Chem. Mater.* **2013**, *25*, 3808–3815.

(8) Liu, J.; Cai, Y.; Deng, Y.; Sun, Z.; Gu, D.; Tu, B.; Zhao, D. Magnetic 3-D ordered macroporous silica templated from binary colloidal crystals and its application for effective removal of microcystin. *Microporous Mesoporous Mater.* **2010**, *130*, 26–31.

(9) Zhang, G.; Wang, D.; Gu, Z.-Z.; Möhwald, H. Fabrication of superhydrophobic surfaces from binary colloidal assembly. *Langmuir* **2005**, *21*, 9143–9148.

(10) Talapin, D. V.; Shevchenko, E. V.; Bodnarchuk, M. I.; Ye, X.; Chen, J.; Murray, C. B. Quasicrystalline order in self-assembled binary nanoparticle superlattices. *Nature* **2009**, *461*, 964–967.

(11) Wang, J.; Ahl, S.; Li, Q.; Kreiter, M.; Neumann, T.; Burkert, K.; Knoll, W.; Jonas, U. Structural and optical characterization of 3D binary colloidal crystal and inverse opal films prepared by direct co-deposition. *J. Mater. Chem.* **2008**, *18*, 981–988.

(12) Liu, G.; Li, X.; Wang, W.; Zhou, F.; Duan, G.; Li, Y.; Xu, Z.; Cai, W. Gold binary-structured arrays based on monolayer colloidal crystals and their optical properties. *Small* **2014**, *10*, 2374–2381.

(13) Utgenannt, A.; Maspero, R.; Fortini, A.; Turner, R.; Florescu, M.; Jeynes, C.; Kannaras, A. G.; Muskens, O. L.; Sear, R. P.; Keddie, J. L. Fast assembly of gold nanoparticles in large-area 2D nanogrids using one-step, near-infrared radiation-assisted evaporation process. *ACS Nano* **2016**, *10*, 2232–2242.

(14) Li, Y.; Koshizaki, N.; Wang, H.; Shimizu, Y. Untraditional approach to complex hierarchical periodic arrays with trinary stepwise architectures of micro-, submicro-, and nanosized structures based on binary colloidal crystals and their fine structure enhanced properties. *ACS Nano* **2011**, *5*, 9403–9412.

(15) Wang, L.; Wan, Y.; Li, Y.; Cai, Z.; Li, H.-L.; Zhao, X. S.; Li, Q. Binary colloidal crystals fabricated with a horizontal deposition method. *Langmuir* **2009**, *25*, 6753–6759.

(16) Dai, Z.; Li, Y.; Duan, G.; Jia, L.; Cai, W. Phase diagram, design of monolayer binary colloidal crystals, and their fabrication based on ethanol-assisted self-assembly at the air/water interface. *ACS Nano* **2012**, *6*, 6706–6716.

(17) Huang, X.; Zhou, J.; Fu, M.; Li, B.; Wang, Y.; Zhao, Q.; Yang, Z.; Xie, Q.; Li, L. Binary colloidal crystals with a wide range of size ratios via template-assisted electric-field-induced assembly. *Langmuir* **2007**, *23*, 8695–8698.

(18) Hoffman, P. D.; Sarangapani, P. S.; Zhu, Y. Dielectrophoresis and AC-induced assembly in binary colloidal suspensions. *Langmuir* **2008**, *24*, 12164–12171.

(19) Zhou, Z.; Yan, Q.; Li, Q.; Zhao, X. S. Fabrication of binary colloidal crystals and non-close-packed structures by a sequential self-assembly method. *Langmuir* **2007**, *23*, 1473–1477.

(20) Jiang, P.; Bertone, J. F.; Hwang, K. S.; Colvin, V. L. Single-crystal colloidal multilayers of controlled thickness. *Chem. Mater.* **1999**, *11*, 2132–2140.

(21) Wang, J.; Li, Q.; Knoll, W.; Jonas, U. Preparation of multilayered trimodal colloid crystals and binary inverse opals. *J. Am. Chem. Soc.* **2006**, *128*, 15606–15607.

(22) Jiang, P.; McFarland, M. J. Large-scale fabrication of wafer-scale colloidal crystals, macroporous polymers, and nanocomposites by spin-coating. *J. Am. Chem. Soc.* **2004**, *126*, 13778–13786.

(23) Yu, J.; Yan, Q.; Shen, D. Co-self-assembly of binary colloidal crystals at the air-water interface. *ACS Appl. Mater. Interfaces* **2010**, *2*, 1922–1926.

(24) Pozzo, D. C.; Walker, L. M. Shear orientation of nanoparticle arrays templated in a thermoreversible block copolymer micellar crystal. *Macromolecules* **2007**, *40*, 5801–5811.

(25) Schaak, R. E.; Cable, R. E.; Leonard, B. M.; Norris, B. C. Colloidal crystal microarrays and two-dimensional superstructures: A versatile approach for patterned assembly. *Langmuir* **2004**, *20*, 7293–7297.

(26) Duan, G.; Cai, W.; Luo, Y.; Lv, F.; Yang, J.; Li, Y. Design and electrochemical fabrication of gold binary ordered micro/nano-structured porous arrays via step-by-step colloidal lithography. *Langmuir* **2009**, *25*, 2558–2562.

(27) Choi, H. K.; Im, S. H.; Park, O. O. Fabrication of unconventional colloidal self-assembled structures. *Langmuir* **2010**, *26*, 12500–12504.

(28) Shimmin, R. G.; DiMauro, A. J.; Braun, P. V. Slow vertical deposition of colloidal crystals: a langmuir-blodgett process? *Langmuir* **2006**, *22*, 6507–6513.

(29) Diao, J. J.; Hutchison, J. B.; Luo, G.; Reeves, M. E. Theoretical analysis of vertical colloidal deposition. *J. Chem. Phys.* **2005**, *122*, 184710–5.

(30) Li, H.-L.; Marlow, F. Solvent effects in colloidal crystal deposition. *Chem. Mater.* **2006**, *18*, 1803–1810.

(31) Kozina, A.; Diaz-Leyva, P.; Palberg, T.; Bartsch, E. Crystallization kinetics of colloidal binary mixtures with depletion attraction. *Soft Matter* **2014**, *10*, 9523–9533.

DOI: 10.1021/acs.langmuir.7b02553
Langmuir 2017, 33, 10366–10373

(32) Kumnorkaew, P.; Gilchrist, J. F. Effect of nanoparticle concentration on the convective deposition of binary suspensions. *Langmuir* **2009**, *25*, 6070−6075.
(33) Kuai, S.-L.; Hu, X.-F.; Haché, A.; Truong, V.-V. High-quality colloidal photonic crystals obtained by optimizing growth parameters in a vertical deposition technique. *J. Cryst. Growth* **2004**, *267*, 317−324.
(34) Hunt, N.; Jardine, R.; Bartlett, P. Superlattice formation in mixtures of hard-sphere colloids. *Phys. Rev. E: Stat. Phys., Plasmas, Fluids, Relat. Interdiscip. Top.* **2000**, *62*, 900−913.
(35) Rugge, A.; Tolbert, S. H. Effect of electrostatic interactions on crystallization in binary colloidal films. *Langmuir* **2002**, *18*, 7057−7065.
(36) Wong, S.; Kitaev, V.; Ozin, G. Colloidal Crystal Films: Advances in Universality and Perfection. *J. Am. Chem. Soc.* **2003**, *125*, 15589−15598.
(37) Vogel, N.; Retsch, M.; Fustin, C.-A.; del Campo, A.; Jonas, U. Advances in colloidal assembly; the design of structure and hierarchy in two and three dimensions. *Chem. Rev.* **2015**, *115*, 6265−6311.
(38) Zheng, J.; Dai, Z.; Mei, F.; Xiao, X.; Liao, L.; Wu, W.; Zhao, X.; Ying, Y.; Jiang, C. Micro-nanosized nontraditional evaporated structures based on closely-packed monolayer binary colloidal crystals and their fine structure enhanced properties. *J. Phys. Chem. C* **2014**, *118*, 20521−20528.
(39) Sakamoto, Y.; Kuroda, Y.; Toko, S.; Ikeda, T.; Matsui, T.; Kuroda, K. Electron microscopy study of binary nanocolloidal crystals with ico-AB_{13} structure made of monodisperse silica nanoparticles. *J. Phys. Chem. C* **2014**, *118*, 15004−15010.
(40) Kuroda, Y.; Sakamoto, Y.; Kuroda, K. Selective cleavage of periodic mesoscale structures: Two-dimensional replication of binary colloidal crystals into dimpled gold nanoplates. *J. Am. Chem. Soc.* **2012**, *134*, 8684−8692.
(41) Yang, L.; Wang, J.; Zhang, Y.; Luo, Y.; Li, D.; Meng, Q. In situ optical microspectroscopy monitoring of binary colloidal crystal growth dynamics via evaporation-induced cooperative self-assembly. *Langmuir* **2012**, *28*, 4160−4167.
(42) Kung, S.-C.; Chang, C.-C.; Fan, W.; Snyder, M. A. Template-free ordered mesoporous silicas by binary nanoparticle assembly. *Langmuir* **2014**, *30*, 11802−11811.
(43) Bartlett, P.; Ottewill, R. H.; Pusey, P. N. Freezing of binary mixtures of colloidal hard spheres. *J. Chem. Phys.* **1990**, *93*, 1299−1312.
(44) Kim, J. J.; Li, Y.; Lee, E. J.; Cho, S. O. Fabrication of size-controllable hexagonal non-close-packed colloidal crystals and binary colloidal crystals by pyrolysis combined with plasma-electron coirradiation of polystyrene colloidal monolayer. *Langmuir* **2011**, *27*, 2334−2339.
(45) Yokoi, T.; Sakamoto, Y.; Terasaki, O.; Kubota, Y.; Okubo, T.; Tatsumi, T. Periodic arrangement of silica nanospheres assisted by amino acids. *J. Am. Chem. Soc.* **2006**, *128*, 13664−13665.
(46) Davis, T. M.; Snyder, M. A.; Krohn, J. E.; Tsapatsis, M. Nanoparticles in lysine—silica sols. *Chem. Mater.* **2006**, *18*, 5814−5816.
(47) Fan, W.; Snyder, M. A.; Kumar, S.; Lee, P.-S.; Yoo, W. C.; McCormick, A. V.; Penn, R. L.; Stein, A.; Tsapatsis, M. Hierarchical nanofabrication of microporous crystals with ordered meoporosity. *Nat. Mater.* **2008**, *7*, 984−991.
(48) Hartlen, K. D.; Athanasopoulos, A. P. T.; Kitaev, V. Facile preparation of highly monodisperse small silica spheres (15 to > 200 nm) suitable for colloidal templating and formation of ordered arrays. *Langmuir* **2008**, *24*, 1714−1720.
(49) Bogush, G. H.; Tracy, M. A.; Zukoski, C. F. Preparation of monodisperse silica particles: Control of size and mass fraction. *J. Non-Cryst. Solids* **1988**, *104*, 95−106.
(50) Chung, Y.-W.; Leu, I.-C.; Lee, J.-H.; Hon, M.-H. Influence of humidity on the fabrication of high-quality colloidal crystals via a capillary-enhanced process. *Langmuir* **2006**, *22*, 6454−6460.
(51) Greenspan, L. Humidity fixed points of binary saturated aqueous solutions. *J. Res. Natl. Bur. Stand., Sect. A* **1977**, *81A*, 89−96.
(52) Eldridge, M. A.; Madden, P. A.; Frenkel, D. A computer simulation investigation into the stability of the AB_2 superlattice in a binary hard sphere system. *Mol. Phys.* **1993**, *80*, 987−995.
(53) Schofield, A. B.; Pusey, P. N.; Radcliffe, P. Stability of the binary colloidal crystals AB_2 and AB_{13}. *Phys. Rev. E* **2005**, *72*, 031407−10.
(54) Bartlett, P.; Ottewill, R. H.; Pusey, P. N. Superlattice formation in binary mixtures of hard-sphere colloids. *Phys. Rev. Lett.* **1992**, *68*, 3801−3804.
(55) Eldridge, M. D.; Madden, P. A.; Frenkel, D. Entropy-driven formation of a superlattice in a hard-sphere binary mixture. *Nature* **1993**, *365*, 35−37.
(56) Eldridge, M. D.; Madden, P. A.; Pusey, P. N.; Bartlett, P. Binary hard-sphere mixtures: a comparison between computer simulation and experiment. *Mol. Phys.* **1995**, *84*, 395−420.
(57) Yamaki, M.; Higo, J.; Nagayama, K. Size-dependent separation of colloidal particles in two-dimensional convective self-assembly. *Langmuir* **1995**, *11*, 2975−2978.
(58) Fortini, A.; Martín-Fabiani, I.; Lesage; De La Haye, J.; Dugas, P.-Y.; Lansalot, M.; D'Agosto, F.; Bourgeat-Lami, E.; Keddie, J. L.; Sear, R. P. Dynamic stratification in drying films of colloidal mixtures. *Phys. Rev. Lett.* **2016**, *116*, 118301−8.

DOI: 10.1021/acs.langmuir.7b02553
Langmuir 2017, 33, 10366−10373